



**HAL**  
open science

# Stress release-induced interfacial twin boundary $\omega$ phase formation in a $\beta$ type Ti-based single crystal displaying stress-induced $\alpha''$ martensitic transformation

Y. Yang, P. Castany, E. Bertrand, M. Cornen, J.X. Lin, T. Gloriant

## ► To cite this version:

Y. Yang, P. Castany, E. Bertrand, M. Cornen, J.X. Lin, et al.. Stress release-induced interfacial twin boundary  $\omega$  phase formation in a  $\beta$  type Ti-based single crystal displaying stress-induced  $\alpha''$  martensitic transformation. Acta Materialia, 2018, 149, pp.97-107. 10.1016/j.actamat.2018.02.036 . hal-01740146

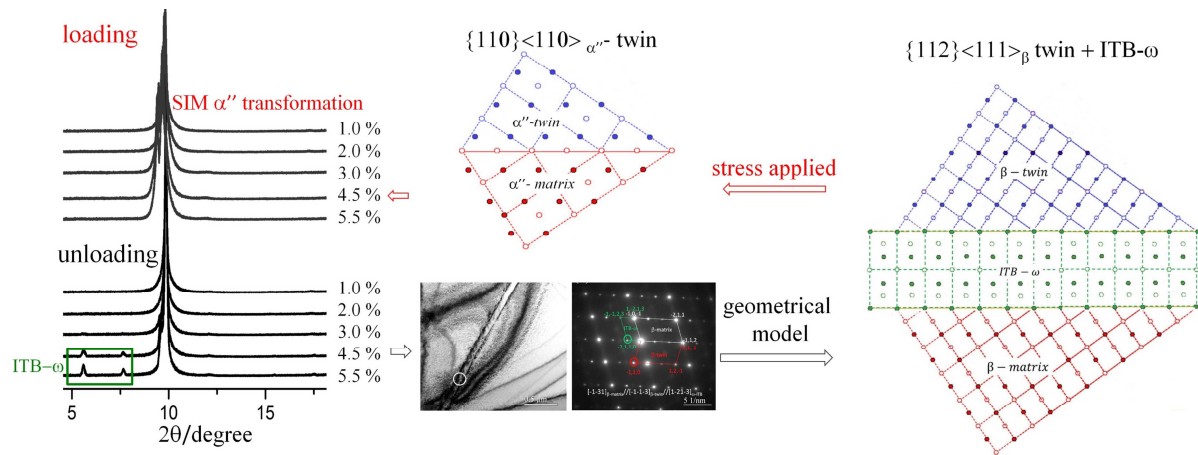
HAL Id: hal-01740146

<https://univ-rennes.hal.science/hal-01740146>

Submitted on 6 Jul 2018

**HAL** is a multi-disciplinary open access archive for the deposit and dissemination of scientific research documents, whether they are published or not. The documents may come from teaching and research institutions in France or abroad, or from public or private research centers.

L'archive ouverte pluridisciplinaire **HAL**, est destinée au dépôt et à la diffusion de documents scientifiques de niveau recherche, publiés ou non, émanant des établissements d'enseignement et de recherche français ou étrangers, des laboratoires publics ou privés.



# 1 Stress release-induced interfacial twin boundary $\omega$ phase formation in 2 a $\beta$ type Ti-based single crystal displaying stress-induced $\alpha''$ 3 martensitic transformation

4 Y. Yang<sup>a,b,c</sup>, P. Castany<sup>b</sup>, E. Bertrand<sup>d</sup>, M. Cornen<sup>b</sup>, J.X. Lin<sup>a,\*</sup>, T. Gloriant<sup>b,\*\*</sup>

5  
6 <sup>a</sup> Key Laboratory of Optoelectronic Materials Chemistry and Physics, Fujian Institute of Research on the  
7 Structure of Matter, Chinese Academy of Science, Fuzhou 350002, China

8 <sup>b</sup> Univ Rennes, INSA Rennes, CNRS, ISCR - UMR 6226, F-35000 Rennes, France

9 <sup>c</sup> Shenzhen Key Laboratory of Human Tissue Regeneration and Repair, Shenzhen Institute, Peking University,  
10 Shenzhen, 518057, China

11 <sup>d</sup> Institut des Matériaux Jean Rouxel (IMN), Université de Nantes, CNRS, Rue Christian Pauc, BP 50609, 44306  
12 Nantes Cedex 3, France

## 13 Abstract

14 The  $\omega$  phase transformation in numerous group IV transition metals plays a key role to change the  
15 phase stability and modify mechanical properties, although its formation mechanisms and effect to  
16 accommodate strains are still unclear. A  $\langle 1\ 1\ 0 \rangle_{\beta}$  single crystal of  $\beta$ -type Ti-24Nb-4Zr-8Sn alloy  
17 (wt. %) is used to investigate the aforementioned problems. This alloy displays a  $\beta$  to  $\alpha''$   
18 stress-induced martensitic transformation, which is reversible and leads to superelasticity. Profiles  
19 obtained from *in situ* synchrotron X-ray diffraction during cyclic tensile tests reveal definitely the  
20 appearance of  $\omega$  phase due to applied stress releasing after unloading while these identified  $\omega$  peaks  
21 shall vanish totally on subsequent loading. TEM microstructural observations show its morphology  
22 as thin layer locating on the boundary of  $\{1\ 1\ 2\}\langle 1\ 1\ 1 \rangle_{\beta}$  twins coinciding well with the feature of  
23 interfacial twin boundary (ITB)  $\omega$  phase, which is proved to be formed passively during the  
24 reversion of  $\{1\ 1\ 0\}\langle 1\ 1\ 0 \rangle_{\alpha''}$  twins. The martensitic twinning components of  $\{1\ 1\ 0\}\langle 1\ 1\ 0 \rangle_{\alpha''}$  are  
25 indeed confirmed from crystallographic reconstructions based on the orientation relationship  
26 between the  $\beta$  and  $\alpha''$  phases. A geometrical model is hence schematically used to analyze in details  
27 the orientation relationships between both deformation  $\{1\ 1\ 2\}\langle 1\ 1\ 1 \rangle_{\beta}$  twins and ITB- $\omega$  phase, as  
28 well as with the original  $\{1\ 1\ 0\}\langle 1\ 1\ 0 \rangle_{\alpha''}$  twinning.

29 **Keywords:** ITB- $\omega$  phase, deformation twinning,  $\{1\ 1\ 2\}\langle 1\ 1\ 1 \rangle_{\beta}$ ,  $\{1\ 1\ 0\}\langle 1\ 1\ 0 \rangle_{\alpha''}$ , interfacial

\* Corresponding author. E-mail address: franklin@fjirsm.ac.cn (J.X. Lin)

\*\* Corresponding author. E-mail addresses: thierry.gloriant@insa-rennes.fr (T. Gloriant)

30 phase, stress-induced martensitic transformation.

## 31 1. Introduction

32 Metastable  $\beta$ -type titanium based alloys are currently developed for applications in medicine  
33 and aerospace. Phase transformations from the body-centered cubic  $\beta$  phase (Im-3m, N<sup>o</sup> 229) to  
34 base-centered orthorhombic  $\alpha''$  phase (Cmcm, N<sup>o</sup> 63) and hexagonal  $\omega$  phase (P6/mmm, N<sup>o</sup> 191)  
35 are observed to be formed leading to several particular properties, such as superelasticity and shape  
36 memory effect. Although the stress-induced  $\alpha''$  phase transformation from  $\beta$  phase has been widely  
37 studied with the classic theory of martensitic crystallography (PTMC) [1-3], the role of  $\omega$  phase was  
38 not clearly established. Especially, the importance of  $\omega$  phase to accommodate internal strains in  
39 alloys, its effect on martensitic  $\alpha''$  phase transformation and the role as precursor for stable  $\alpha$  phase  
40 are still in debates.

41 As brittle particles known to be deleterious on mechanical properties, the isothermal  $\omega$  phase  
42 was firstly identified in aged Ti-Cr alloy [4]. Various external stimulation including rapid cooling  
43 from single  $\beta$  phase field in high temperature range, mechanical deformation, extremely high  
44 pressure and exposure to radiation were then claimed to enable the inducement of the  $\omega$  phase in  
45 numerous group IV transition metals (Ti, Ta, Hf and Zr) based alloys [5-9]. Depending on different  
46 historical processes, the particle morphologies of  $\omega$  phase can be ellipsoidal or cuboidal after ageing  
47 [10-12] and plate-like in strained titanium alloys [13-15]. These morphological differences for  $\omega$   
48 phase can be attributed to both compositional partition and stressing condition [10-12, 16-18].  
49 However, the model of collapsing one pair of  $\{1\ 1\ 1\}_{\beta}$  planes to an intermediate position leaving the  
50 adjacent  $\{1\ 1\ 1\}_{\beta}$  planes unaltered were proved and widely accepted as the formation mechanism of  
51  $\omega$  phase for nearly all cases [3, 19, 20]. Amongst them, thin layer  $\omega$  phase located along the twin  
52 boundary, which was called ITB- $\omega$  [18], deserves more investigation. The two twinning systems  
53 observed in  $\beta$ -type Ti alloys are  $\{1\ 1\ 2\} \langle 1\ 1\ 1 \rangle_{\beta}$  [18, 19, 21-25] and  $\{3\ 3\ 2\} \langle 1\ 1\ 3 \rangle_{\beta}$  [26-31]. In a  
54 recent work carried out in a Ti-Nb alloy [18], the formation of ITB- $\omega$  was observed due to a  
55 collapsing process of the  $\{3\ 3\ 2\}_{\beta}$  twin planes. The formation of such ITB- $\omega$  phase along  $\{3\ 3\ 2\}$   
56  $\langle 1\ 1\ 3 \rangle_{\beta}$  twins was also shown to be intrinsically due to the reverse  $\alpha''$  to  $\beta$  transformation and the  
57 subsequent stress relaxation along twin boundaries.

58 Such kind of ITB- $\omega$  phase was also observed in the vicinity of the  $\{1\ 1\ 2\} \langle 1\ 1\ 1 \rangle_{\beta}$  twin  
59 boundaries in a deformed Ti-15Mo-5Zr (at. %) alloy [32]. Further,  $\omega$ -phase with a zigzag  
60 morphology was observed in a Ti-34Nb (at. %) alloy and its formation was proposed to be featured

61 by three-layer lattice shears arising from the dissociation and cross-slip of screw dislocations on  
62 consecutive  $\{1\ 1\ 2\}_\beta$  planes [23]. A detailed dislocation mechanism using the dissociation of the  
63 core of  $1/2 \langle 1\ 1\ 1 \rangle_\beta$  dislocations into three  $1/6 \langle 1\ 1\ 1 \rangle_\beta$  twinning dislocations and  $1/12 \langle 1\ 1\ 1 \rangle_\beta$ ,  
64  $1/3 \langle 1\ 1\ 1 \rangle_\beta$  and  $1/12 \langle 1\ 1\ 1 \rangle_\beta$  transition dislocations was described for interpretation of the  
65 mentioned boundary complexions [21]. Another mechanism was proposed from first principle  
66 calculations coupling with microstructural observations in the Ti-30Nb-3Pd (at. %) alloy: The  
67 nucleation and growth of  $\{1\ 1\ 2\} \langle 1\ 1\ 1 \rangle_\beta$  twins can be described on the basis of the reverse  
68 transformation of  $\omega$  phase into  $\beta$  phase [24, 33]. With such a mechanism,  $\{1\ 1\ 2\} \langle 1\ 1\ 1 \rangle_\beta$  twins are  
69 formed inside  $\omega$  particles and the ITB- $\omega$  phase observed along twin boundaries are the  
70 untransformed part of  $\omega$  particles involved in the twinning process. The formation of ITB- $\omega$  phase  
71 along  $\{1\ 1\ 2\} \langle 1\ 1\ 1 \rangle_\beta$  twin boundaries is thus mainly describe from mechanisms which do not  
72 consider the  $\beta$ - $\alpha'$  transformation. But the comprehensive participation of martensitic  $\alpha'$   
73 transformation and  $\{1\ 1\ 2\} \langle 1\ 1\ 1 \rangle_\beta$  deformation twins on the formation mechanism for the ITB- $\omega$   
74 phase is of great interest and a deeper understanding on the formation sequence or mediation details  
75 have never been reported.

76 In the present work, a  $\beta$ -type titanium based alloy with the chemical composition of  
77 Ti-24Nb-4Zr-7.9Sn (wt. %, short for Ti2448 thereafter) was investigated. This Ti2448 alloy was  
78 firstly designed for biomedical implants and prostheses because it exhibits a Young's modulus as  
79 low as 42 GPa and a superelastic behavior characterized by a maximum recoverable strain of 3.3%  
80 [25, 34-39]. As the origin of superelasticity, the stress-induced  $\alpha'$  martensitic transformation was  
81 evidenced in polycrystalline deformed specimens [37]. In the present case, a  $\langle 1\ 1\ 0 \rangle_\beta$  single crystal  
82 of this Ti2448 alloy was elaborated to simplify the microstructure. *In situ* synchrotron X-ray  
83 diffraction (SXRD) under cyclic tensile test were used to detect the stress-induced martensitic  $\alpha'$   
84 phase transformation and ITB- $\omega$  phase formation. Further TEM and orientation analysis were  
85 performed to reveal the transformation details. A new deformation sequence for deformation  $\beta$   
86 twinning and ITB- $\omega$  formation, as well as the relevant geometrical model indicating the change of  
87 the crystallographic lattice were finally obtained.

## 88 2. Materials and methods

89 Ingot of Ti-24Nb-4Zr-8Sn (wt. %) alloy with diameter of 55 mm was made by arc melting under  
90 argon and hot forged at 1273 K into 25 mm diameter bar. A cylinder of 8.6 mm in diameter was cut  
91 from the as-forged bar and used to grow seed-crystal rods in an optical floating-zone furnace  
92 (FZ-T-12000-X-VP-S, Crystal System Inc.) under the protection of flowing argon. The growth was

93 carried out at a rate of  $5 \text{ mm.h}^{-1}$  and a rotation rate of 25 rpm. The seed crystal was cut along the  
94  $\langle 110 \rangle_{\beta}$  direction after the orientation was determined by both X-ray diffraction (XRD) and Laue  
95 X-ray back reflection analyses within  $1^{\circ}$  of the desired orientation and then used to grow  
96 single-crystal rods. The orientation of the grown single crystal was also confirmed by Laue X-ray  
97 back reflection analysis. XRD and transmission electron microscopy (TEM) were used to examine  
98 the single  $\beta$  phase and confirm the absence of formation of both  $\omega$  phase and  $\alpha''$  martensitic phase.  
99 Chemical analyses showed that the grown crystals has a similar composition compared to the forged  
100 bar.

101 Cyclic tensile test at room temperature consisting of strain increments of 0.5 % followed by  
102 stress release up to an elongation of 5.5 % was conducted with an INSTRON 3369 tensile machine  
103 (strain rate:  $10^{-4} \text{ s}^{-1}$ ). An extensometer was used to ensure the accurate control of the strain. The  
104 tensile direction was chosen parallel to the single crystal growth direction, i.e. the  $\langle 110 \rangle_{\beta}$   
105 direction. In order to observe the deformed microstructure, single crystal specimens were cut after  
106 tensile tests and prepared by mechanically grinding with increasing grades of SiC abrasive paper,  
107 then polished with colloidal silica suspension and finally etched in a solution composed of 8 % HF,  
108 15 %  $\text{HNO}_3$  and 77 %  $\text{H}_2\text{O}$  (vol. %). Further observations were conducted using a JEOL 2100  
109 transmission electron microscope (TEM) operating at 200 kV. Thin foils for TEM observations  
110 were cut as disks of 3 mm in diameter, further polished to a thickness of 150  $\mu\text{m}$  and prepared by a  
111 twin-jet electro-polishing technique with a 6 % perchloric acid and 94 % methanol (vol. %) solution  
112 at  $-25^{\circ}\text{C}$ . Twin-jet electro-polishing was stopped before perforation and the samples were finally  
113 thinned by ion milling with a Fischione 1010 Model.

114 *In situ* synchrotron X-ray diffraction (SXR) under cyclic tensile test was conducted on beam  
115 line ID31 at the European Synchrotron Radiation Facility (ESRF, Grenoble, France) with a 5 kN  
116 micro-tensile dispositive. The high-resolution ID31 beamline offers a high-energy incident X-ray  
117 beam ( $\lambda = 0.040002106 \text{ nm}$ ) coupled with a nine-channel multi-analyzer installed as detectors. The  
118 transmitted diffracted beams were collected over the  $\theta$  angular range  $2\text{--}14^{\circ}$  with a scanning step of  
119  $0.005^{\circ}$ . The *in situ* cyclic tensile tests under synchrotron radiation were realized on the same single  
120 crystal tensile specimen (gauge width of 3 mm and a thickness of 0.5 mm) with increments of 0.5 %  
121 until 5.5 %. SXR scans were therefore obtained after each strain increment for both loading and  
122 unloading conditions. More details about the setup configuration can be found in reference [40].

## 123 3. Results

### 124 3.1. Tensile test

125 Fig.1 displays the cyclic tensile curve from 0 to 5.5 % strain for the  $\langle 1\ 1\ 0 \rangle_{\beta}$  single crystal. On  
126 this curve, large hysteresis loops can be clearly observed due to the stress-induced martensitic  
127 transformation (SIM) occurring. Indeed, after the linear elasticity of the  $\beta$  phase, a stress plateau  
128 can be noticed in the strain range of 0.75 ~ 3 % which corresponds to the main stage of SIM  $\alpha''$   
129 transformation. Thus, the critical stress for the SIM  $\alpha''$  transformation can be evaluated to be 250  
130 MPa with the method of intersection point between two tangent lines. After 3 % of strain, the  
131 martensitic  $\alpha''$  phase begins to deform elastically followed by its plastic deformation. The  
132 recoverable strains used to evaluate the superelasticity at different applied strains are measured with  
133 the method illustrated in reference [41] and displayed with black open circles according to the right  
134 vertical axis. It can be noticed that the recoverable strain increases linearly with the applied strain  
135 up to 4 % of strain. Up to this value, the applied strain can be totally recovered due to the  
136 reversibility of the SIM  $\alpha''$  transformation. On the other hand, the incipient Young's modulus and  
137 the ultimate tensile strength are measured to be 51 GPa and 623 MPa, respectively.

### 138 3.2. *In situ* SXRD characterization

139 Fig. 2a presents the whole SXRD profiles of the single crystal during the cyclic tensile test on  
140 loading (upper in red) and after unloading (lower in black) between 0 and 5.5 % of applied strain.  
141 On the first initial profile, only  $(1\ 1\ 0)_{\beta}$  and  $(2\ 2\ 0)_{\beta}$  peaks are detected, which is in accordance with  
142 the  $\langle 1\ 1\ 0 \rangle_{\beta}$  single crystalline state. When the applied strain increases, SIM  $\alpha''$  transformation  
143 occurs. However, the diffracted peaks belonging to  $\alpha''$  phase are very close to the  $\{1\ 1\ 0\}_{\beta}$  and  $\{2\ 2\ 0\}_{\beta}$   
144 peaks that is why three enlarged angle ranges from Fig. 2a are presented in Fig. 2b, 2c and 2d  
145 for a better identification of the phase evolution.

146 In the Fig. 2b that shows profiles on loading, it can be noticed that the  $(1\ 1\ 0)_{\beta}$  peak slightly  
147 shifts to the low angles due to the elastic expansion of the  $\beta$  lattice until the detection of the  $(0\ 2\ 0)_{\alpha''}$   
148 diffraction peak when the applied strain reaches 1 %. Then, the other typical diffraction peaks of  
149  $(0\ 0\ 2)_{\alpha''}$  and  $(1\ 1\ 1)_{\alpha''}$  appear at higher applied strain. Once the strain exceeds 3 %, the  $\beta$  phase  
150 seems to disappear totally that will be confirmed hereafter from the calculation of transformation  
151 strains. This assumption is highlighted by the vanishing of  $(1\ 1\ 0)_{\beta}$  peak replaced by the  
152 superimposition of the three  $(0\ 2\ 0)_{\alpha''}$ ,  $(0\ 0\ 2)_{\alpha''}$  and  $(1\ 1\ 1)_{\alpha''}$  diffraction peaks. Under the

153 corresponding unloading conditions in Fig. 2c, nearly all the diffraction peaks of the  $\alpha''$  phase  
154 disappear while the peak of the  $\beta$  phase appears back, showing the  $\alpha''$  phase reverses back to its  
155 parent  $\beta$  phase before the strain reaches 3.5 %. Positions of peaks of  $\alpha''$  phase are also indicated, but  
156 the quantity of residual martensite is negligible for the 3.5% condition, while its presence is more  
157 obvious at higher strain, even if the  $\beta$  phase is the main phase remaining after unloading. Moreover,  
158 the reversed  $(1\ 1\ 0)_\beta$  peak and remaining peaks of  $\alpha''$  (when there are) keep in the same position,  
159 implying that the shift of all peaks observed on loading is due to the elasticity of the two phases.  
160 For profiles under the unloading condition released from a higher applied strains at 4.5 ~ 5.5 % in  
161 Fig. 2c, diffraction peaks of  $(0\ 0\ 2)_{\alpha''}$  and  $(1\ 1\ 1)_{\alpha''}$  with tiny intensity are left around the main  $(1\ 1$   
162  $0)_\beta$  peak. This is because the SIM  $\alpha''$  transformation cannot be totally reversed due to the onset of  
163 plastic deformation which inhibits the reverse martensitic transformation.

164 Another interesting phenomenon can be noticed in Fig. 2d. Indeed, two small but  
165 well-identified peaks at  $5.6^\circ$  and  $7.6^\circ$  are clearly visible. However, they cannot be indexed from any  
166  $\alpha''$  or  $\beta$  phases. In fact, these two peaks can be indexed as the  $(0\ 1\ -1\ 0)_\omega$  and  $(0\ 0\ 0\ 1)_\omega$  planes of  
167 the  $\omega$  phase, which is also a common observed phase in both deformed and quenched metastable  
168 Ti-based alloys. Such a formation of  $\omega$  phase when the stress is released from the plastic  
169 deformation domain was never reported and the reason of its appearance will be explicated further  
170 from the microstructural analysis.

171 The deformation sequence of the present  $\langle 1\ 1\ 0 \rangle_\beta$  single crystal can be therefore extracted on  
172 the basis of both the SXRD profiles and analysis of cyclic tensile curves in the Fig. 1. The  
173 deformation begins from pure elastic deformation of  $\beta$  phase. At the 0.5 % strain, the SIM  $\alpha''$  starts  
174 to occur and continues to coexist with the elastic deformation of the  $\beta$  phase until the fulfillment of  
175 the phase transformation at 3 % strain. At the strain range of 3 ~ 4.5 %, the SIM  $\alpha''$  phase deforms  
176 elasticity then stepped into a complete plastic deformation range of 4.5 ~5.5 % characterized by the  
177 stabilization of permanent deformation. During this last step, an unexpected formation of  $\omega$  phase  
178 after releasing the stress is also evidenced.

179 Evolutions of the cell parameters of  $\beta$  and SIM  $\alpha''$  phases are also determined from the  
180 diffraction profiles and are plotted in Fig. 3 as a function of the applied percentage strain under  
181 loading conditions. The lattice parameter of  $\beta$  phase is continuously increasing when the strain  
182 increases until 3 % strain on loading while keeps constant after unloading. For the SIM  $\alpha''$  phase,  
183 the  $b_{\alpha''}$  and  $c_{\alpha''}$  parameters continuously increases when the strain increases while the  $a_{\alpha''}$  parameter  
184 is roughly constant. It is also worth noting that lattice parameters of the  $\alpha''$  phase cannot be properly  
185 determined for applied strain smaller than 3 % due to a limited number of diffraction peaks

186 although SIM  $\alpha''$  transformation already occurs. The cell parameters of  $\beta$  phase, SIM  $\alpha''$  phase and  
 187  $\omega$  phase, which are determined within the plastic deformation range after unloading, are presented  
 188 in Table 1. These values are used to calculate the phase transformation strains for each possible  
 189 variants of  $\alpha''$  martensite (Table 2). As generally assumed, this is the variant leading to the  
 190 maximum of transformation strain that would be formed, i.e. the CV3 here with a value of about  
 191 4.3%. This means the recoverable strain would be measured as 4.3% if all the  $\beta$  phase transforms  
 192 into  $\alpha''$  martensite with a full reversibility after unloading. As the maximum recoverable strain was  
 193 indeed measured as 4.3% (Fig. 1), one can conclude that all the  $\beta$  phase is transformed during  
 194 deformation as assumed from the description of SXRD results (Fig. 2).

### 195 3.3. Microstructural observations

196 An example of the plastically deformed microstructure observed by optical microscopy for a  
 197 sample deformed at 4.5 % is presented in Fig. 4. Two groups of deformation bands crossed with  
 198 each others can be clearly observed on this micrograph. In order to determine the nature of these  
 199 bands, TEM observations were carried out.

200 Fig. 5 shows the TEM observations of the single crystal deformed at 4.5 % strain. The bright  
 201 field image (BFI) in Fig. 5a presents dislocation pile-ups indicating the involvement of dislocation  
 202 slip. The selected area electron diffraction (SAED) of Fig. 5b corresponding to the circled area of  
 203 the matrix in Fig. 5a was indexed as the  $\beta$  phase with the  $[1\ 1\ 3]_{\beta}$  zone axis. A careful analysis of  
 204 the slip trace on the Fig. 5a according to the crystallographic orientation of the single crystal shows  
 205 the dislocations slip in a  $\{1\ 1\ 0\}_{\beta}$  plane (more details about the method can be found in reference  
 206 [42]). This result is consistent with the most common slip planes observed in the  $\beta$  phase of  
 207 titanium alloys but also in other bcc alloys [43-45]. A BFI from another typical area is presented in  
 208 Fig. 5c and its corresponding SAED in Fig. 5d. It can be seen the superimposition of three sets of  
 209 diffraction patterns marked by different colors on the SAED. After indexation, the deformation  
 210 bands observed in Fig. 5c correspond clearly to the  $\{1\ 1\ 2\}\langle 1\ 1\ 1\rangle_{\beta}$  twinning system but additional  
 211  $\omega$  phase diffracted spots are also observed sharing the common zone axis for  $[1\ 1\ 0]_{\beta\text{-matrix}} // [1\ 1\ 0]_{\beta\text{-twin}} // [-1\ -1\ 2\ 0]_{\omega}$ .

213 The TEM observations of another area in Fig. 6a and 6b also confirms the formation of plastic  
 214  $\{1\ 1\ 2\}\langle 1\ 1\ 1\rangle_{\beta}$  twins and the formation of  $\omega$  phase but with a different diffracting condition  
 215 corresponding to  $[-1\ -3\ 1]_{\beta\text{-matrix}} // [-1\ -1\ -3]_{\beta\text{-twin}} // [1\ -2\ 1\ -3]_{\omega}$  zone axis. It can be noticed that, for  
 216 this specific orientation, the common  $\{1\ 1\ 2\}$  plane between the twin and the matrix, which can be  
 217 seen on the SAED pattern, is not the twinning plane. The twinning plane will be further indicated in

218 the Fig. 7a and 7b. Diffracted spots related to the twin and  $\omega$  phase are selected and relevant  
219 dark-field images are shown in Fig. 6c and 6d. It is worth noting that the  $\omega$  phase shows a strong  
220 contrast, which allows to observe its localization at the twin boundary. This indicates its nature of  
221 interfacial twin boundary phase (ITB- $\omega$ ). The  $\omega$  phase layer appears here rather thick because the  
222 twin interface is inclined according to the electron beam. Due to the crystallographic orientation of  
223 this twin, it was not possible to get the twin interface edge-on (see Fig. 7a and 7b). It can also be  
224 noticed that such an ITB  $\omega$  phase exhibiting a thin layer morphology was already reported in other  
225  $\beta$ -metastable titanium alloys [16, 18, 19].

226 This ITB  $\omega$  phase is thus the  $\omega$  phase that is detected during the SXRD experiments, as no  
227 nano-sized athermal  $\omega$  phase can be detected from SAED patterns. Indeed, no diffuse streaks are  
228 visible on the  $[113]_{\beta}$  zone axis SAED pattern (Fig. 5b) as commonly observed when precipitation of  
229 athermal  $\omega$  phase occurs during the quench [3, 10, 13]. Therefore, the  $\omega$  phase detected by SXRD is  
230 not athermal  $\omega$  phase initially present in the microstructure but is truly the ITB  $\omega$  phase observed by  
231 TEM along the twin boundaries.

## 232 4. Discussion

233 We showed by SXRD analysis that the microstructure of samples after stress released from the  
234 plastic deformation range consists mainly of  $\beta$  phase with a small amount of residual SIM  $\alpha''$  phase  
235 and ITB- $\omega$  phase. However, the TEM observations on sample released from 4.5 % do not exhibit  
236 any detection of SIM  $\alpha''$  phase. The reason is due to internal stress relaxation occurring during the  
237 thin foil preparation, which is reasonably accepted. The point to elucidate now concerns the  
238 mechanism of the ITB- $\omega$  phase formation. Indeed, this phase is never observed when the sample is  
239 under stress but only when the sample is released after being deformed in the plastic domain  
240 according to our SXRD analyses. The problem is that many transformations occurred in this  
241 metastable alloy such as the stress-induced martensitic transformation, twinning and  $\omega$ -phase  
242 formation, which can be reversible and depend on each other.

243 The SIM  $\alpha''$  transformation was confirmed by SXRD experiments with a phase-transformed  
244 fraction of 100 % when a strain of 4.5 % is reached. That means that the plastic deformation  
245 mechanisms, such as twinning and dislocation slip, occur in this SIM  $\alpha''$  phase and not in the  $\beta$  phase.  
246 Indeed, the plastic deformation starts between 4 and 4.5% of applied strain, as some residual strain  
247 starts to be measured after unloading from 4.5% (Fig. 1). In addition, as the formation of  $\omega$  phase is  
248 observed only after unloading from 4.5% of applied strain, that means the  $\omega$  phase is formed after  
249 plastic deformation has occurred, and thus after twinning of martensite has occurred. It is also worth

250 noting that the  $\omega$  phase is not detected after further loading (5%) but appears again when the stress  
 251 is removed again: The formation of  $\omega$  phase is thus reversible, meaning that the observed twins in  
 252 the  $\beta$  phase with the ITB  $\omega$  phase can transform again into twins in the  $\alpha''$  martensite without any  $\omega$   
 253 phase during subsequent loading. Plastic deformation mechanisms of  $\alpha''$  martensite are not  
 254 exhaustively known but twinning was already reported in the literature as the  $\{1\ 3\ 0\}\langle 3\ 1\ 0\rangle_{\alpha''}$  or  
 255 the  $\{1\ 1\ 0\}\langle 1\ 1\ 0\rangle_{\alpha''}$  twinning systems [46-48]. Therefore, the observed  $\{1\ 1\ 2\}\langle 1\ 1\ 1\rangle_{\beta}$  twins  
 256 combined with the stress release-induced ITB- $\omega$  phase formation is believed to be linked directly  
 257 with the  $\alpha''$  martensitic twinning under stress condition. In order to prove this hypothesis, the  $\alpha''$   
 258 martensitic twinning components has to be detailed on the basis of the well-known orientation  
 259 relationship (OR) between the body-centered cubic  $\beta$  phase and the orthorhombic  $\alpha''$  phase given in  
 260 Table 2 [49]. These data are used to make the crystallographic reconstruction of  $\alpha''$  twins on loading  
 261 from the crystallographic orientations of the  $\beta$  phase observed after the stress is removed.

262 By way of illustration, the crystallographic orientations of the  $\beta$ -matrix and  $\beta$ -twin observed in  
 263 the Fig. 6 are presented on stereographic projections in Fig. 7a and 7b. The common  $(-1\ -2\ -1)_{\beta}$   
 264 twinning plane is indicated as well as the common  $\langle 1\ 1\ 1\rangle_{\beta}$  twinning direction. The corresponding  
 265 crystallographic orientations of matrix and twin after transformation into  $\alpha''$  phase were then  
 266 determined by applying the OR. Actually, six possible orientations of  $\alpha''$ , named variants (V1 to V6)  
 267 were deduced from a certain orientation of  $\beta$ -matrix or  $\beta$ -twin. All the combinations between both  
 268 orientations of matrix and twin were tested in order to identify a potential twinning relationship in  
 269 the  $\alpha''$  phase under stress condition. For that, a rotation of  $180^\circ$  around the potential common  
 270 twinning direction or reflection through the common twinning plane were made to confirm the  
 271 twinning relationship. The tested potential common twinning planes and directions were referenced  
 272 in several articles related to  $\alpha''$  martensite or similar structure in  $\alpha$ -uranium [47, 50-52]. Finally,  
 273 only one convincing possibility was found between the  $\alpha''$ -matrix-V3, and  $\alpha''$ -twin-V3, both  
 274 represented in Fig. 7c and Fig. 7d, respectively. The twinning relationship found here corresponds  
 275 thus to a compound  $\{1\ 1\ 0\}\langle 1\ 1\ 0\rangle_{\alpha''}$  twin.

276 It is demonstrated clearly that the  $\alpha''$ -matrix-V3 and  $\alpha''$ -twin-V3 keep a  $\{1\ 1\ 0\}\langle 1\ 1\ 0\rangle_{\alpha''}$   
 277 twinning relationship, because (i) the two projections share a common  $(-1\ -1\ 0)_{\alpha''}$  pole and a  
 278 common  $[-1\ 1\ 0]_{\alpha''}$  direction indicated in Fig. 7c and 7d and (ii) the operation of a reflection through  
 279 the  $(-1\ -1\ 0)_{\alpha''}$  plane or a rotation of  $180^\circ$  around the  $[-1\ 1\ 0]_{\alpha''}$  direction for the  $\alpha''$ -matrix-V3 leads  
 280 to the orientation of the  $\alpha''$ -twin-V3. Therefore, the  $\alpha''$ -matrix-V3 and  $\alpha''$ -twin-V3 are in the  
 281 compound  $\{1\ 1\ 0\}\langle 1\ 1\ 0\rangle_{\alpha''}$  twinning relationship. Further, the loading direction of the single  
 282 crystal was ascertained as  $[1\ 0\ 1]_{\beta\text{-matrix}}$ . Along this loading direction, the phase transformation strain

283 can be thus calculated according to theory of PTMC [53] and results were presented in Table 2. The  
 284 maximum value is calculated as 4.29 % for V3. As it is generally assumed that the variant that is  
 285 formed during a tensile test is the one giving the maximum of transformation strain, the occurrence  
 286 of V3 is then in good agreement with the orientation of the single crystal of  $\beta$  phase. It can also be  
 287 noticed that, according to the Fig. 1, the residual strain of approx. 0.2 % is measured at the applied  
 288 strain of 4.5 % which is exactly the sum of phase transformation strain (4.29 %) and residual strain  
 289 (0.2 %). Thus, the results of crystallographic reconstruction to determine the twinning system in  $\alpha''$   
 290 martensite are in perfect accordance to the variant selection of  $\alpha''$  due to the external stress.

291 Moreover, the twinning plane  $(-1 -1 0)_{\alpha''}$  and the twinning direction  $[-1 1 0]_{\alpha''}$  indicated in Fig. 7c  
 292 coincide exactly with the twinning plane  $(-1 -2 -1)_{\beta}$  and the twinning direction  $[1 -1 1]_{\beta}$  in Fig. 7a,  
 293 respectively, indicating a clear lattice correspondence between the deduced  $\{1 1 0\}\langle 1 1 0\rangle_{\alpha''}$   
 294 twinning system in the  $\alpha''$  phase and the observed  $\{1 1 2\}\langle 1 1 1\rangle_{\beta}$  twinning system in the relaxed  $\beta$   
 295 phase. The crystallographic orientation of the ITB- $\omega$  phase obtained from the DP in Fig. 6b is also  
 296 shown with a stereographic projection in Fig. 7e. Some interfacial features can be found obviously:  
 297 the twinning planes of  $(-1 -2 -1)_{\beta}$  and  $(-1 -1 0)_{\alpha''}$  are indeed parallel to the  $(0 -1 1 0)_{\omega}$ , while the  
 298 twinning directions of  $[1 -1 1]_{\beta}$  and  $[-1 1 0]_{\alpha''}$  are parallel to the  $[0 0 0 -1]_{\omega}$  of the ITB- $\omega$  phase. The  
 299 present orientation relationship between  $\beta$  and  $\omega$  phase is specific for ITB- $\omega$  phase with a strong  
 300 correlation between the twinning elements and the  $\omega$  phase. Indeed, the twinning plane is parallel to  
 301  $(0 -1 1 0)_{\omega}$  and the twinning direction is parallel to the  $[0 0 0 1]_{\omega}$  direction. This specific orientation  
 302 relationship was already pointed out in a gum metal alloy for the same twinning system [16] and  
 303 also in a Ti-Nb binary alloy for the  $\{3 3 2\}\langle 1 1 3\rangle_{\beta}$  twinning system [18], both exhibiting such  
 304 ITB- $\omega$  phase. An explicit illustration of these orientation relationships is exhibited in Fig. 7f based  
 305 on eighteen unit cells of  $\beta$  phase highlighted with red color. The unit cell of  $\alpha''$  phase and ITB- $\omega$   
 306 phase are then highlighted with blue and green colors, respectively. Moreover, the path for atoms  
 307 displacements which are necessary to realize the phase transformation are marked by hollow atoms  
 308 and corresponding arrows.

309 The release of applied strain from the plastically deformed single crystal causes the reverse  
 310 martensitic transformation, thus the microstructure is observed as the resultant  $\{1 1 2\}\langle 1 1 1\rangle_{\beta}$  type  
 311 with ITB- $\omega$  phase that is formed in order to minimize the surface energy of complex boundaries. As  
 312 reported in a recent work [18], the ITB- $\omega$  phase is assumed to accommodate strains that are  
 313 originated from the reverse martensitic transformation of the  $\{1 3 0\}\langle 3 1 0\rangle_{\alpha''}$  twin boundary into  
 314  $\{3 3 2\}\langle 1 1 3\rangle_{\beta}$  twin interfaces in a metastable  $\beta$ -type Ti-Nb alloy. The ITB- $\omega$  phase formed in the  
 315 present case during the transformation from  $\{1 1 0\}\langle 1 1 0\rangle_{\alpha''}$  twin boundary into  $\{1 1 2\}\langle 1 1 1\rangle_{\beta}$

316 twin actually follows the similar mechanisms but is activated along different crystallographic planes  
317 and directions.

318 The geometrical models for the deformation twinning and ITB- $\omega$  phase are presented in Fig. 8  
319 according to the lattice correspondence in Fig. 7f. The projection of the lattice is chosen to be along  
320 the planes of  $(0\ 0\ -1)_{\alpha''\text{-matrix}} // (0\ 0\ 1)_{\alpha''\text{-twin}} // (-1\ 0\ 1)_{\beta\text{-matrix}} // (1\ 0\ 1)_{\beta\text{-twin}} // (2\ -1\ -1\ 0)_{\text{ITB-}\omega}$ . All solid  
321 circles indicate the atoms in the plane of figure, while the open circles the atoms below the plane of  
322 figure. The red, blue and green atoms refer to the initial lattice, the twinned lattice and the resultant  
323 ITB- $\omega$  lattice, respectively. The Fig. 8a firstly illustrates  $\{1\ 1\ 0\} \langle 1\ 1\ 0 \rangle_{\alpha''}$  twinning formed via  
324 plastic deformation on the basis of fully transformed  $\alpha''$  matrix. The twinning plane  $(-1\ -1\ 0)_{\alpha''\text{-matrix}}$   
325 and twinning direction  $[-1\ 1\ 0]_{\alpha''\text{-matrix}}$  are marked. It is worth noting, that the atomic layers A, B, C  
326 are not at equal distance to each other. The distance between these planes is dependent on the value  
327 of  $y$ , which is a parameter related to the positions of atoms in the orthorhombic cell of the  $\alpha''$  phase.  
328 Its value lies between  $1/6$  and  $1/4$ , while the value  $y=1/6$  describes an hcp structure ( $\alpha$  phase) and  
329 the value  $y=1/4$  describes a bcc structure ( $\beta$  phase).

330 The observed  $\{1\ 1\ 2\} \langle 1\ 1\ 1 \rangle_{\beta}$  twin and ITB- $\omega$  phase which are passively formed after  
331 releasing the stress are also presented in Fig.8b. It can be noticed that the reverse transformation  
332 from  $\alpha''$  to  $\beta$  leads to an equal distance between A, B and C atomic layers. Moreover, these atomic  
333 layers are also equally distanced in the  $\omega$  phase. So, the reverse transformation is helpful to form an  
334 ITB- $\omega$  phase during the phase rerverision. Some atoms have thus to be slightly moved to form the  $\omega$   
335 phase (arrows on the fig. 8b). The final configuration of the twin interface after removing the stress  
336 is then illustrated in the Fig.8c with the orientation relationship between the ITB- $\omega$  phase and both  
337 the twin and matrix of the  $\beta$  phase which are in a  $\{1\ 1\ 2\} \langle 1\ 1\ 1 \rangle_{\beta}$  twinning remationship.

## 338 5. Conclusions

339 The present investigation employed a single crystal with a nominal chemical composition of  
340 Ti-24Nb-4Zr-8Sn (wt. %) to investigate the  $\omega$  phase on the twin boundaries. Techniques including  
341 cyclic tensile test, *in situ* synchrotron X-ray diffraction, TEM observations and crystallographic  
342 orientation reconstruction are used to comprehensively analyze the deformation features. Results as  
343 following are obtained:

- 344 (1) The  $\langle 1\ 1\ 0 \rangle_{\beta}$  Ti2448 single crystal exhibits a maximum recoverable strain of 4.2 % at the  
345 applied strain of 4.5 %. Incipient young's modulus and ultimate tensile strength were  
346 measured to be 51 GPa and 623 MPa. SXR profiles confirmed the superelasticity is due  
347 to phase transformation and cell parameters were thus obtained.

- 348 (2) Surprisingly, apparition of diffracted peaks related to the  $\omega$  phase is found on SXRD  
349 profiles when the stress is removed, only from the plastic deformation range. These peaks  
350 disappear after further loading and appear back after subsequent unloading. The  $\{1\ 1\ 2\}\langle 1\ 1\ 1\rangle_{\beta}$   
351 deformation twinning is identified with diffraction patterns and TEM dark field images.
- 352 (3) Taking the sample deformed up to 4.5 % as an example, the applied strain is accommodated  
353 by martensitic  $\alpha''$  phase transformation strain (4.29 %) and plastic deformation leading to  
354 residual strain after unloading (0.2 %). The TEM analysis also shown the presence of ITB- $\omega$   
355 phase located along twin boundaries. Accordingly to SXRD results, this ITB- $\omega$  phase is  
356 formed when the stress is released.
- 357 (4) From crystallographic reconstruction based on the orientation relationship, results illustrate  
358 that the observed  $\{1\ 1\ 2\}\langle 1\ 1\ 1\rangle_{\beta}$  and ITB- $\omega$  phase are the resultant lattice complexion due  
359 to the reversion of  $\{1\ 1\ 0\}\langle 1\ 1\ 0\rangle_{\alpha''}$  twins. The ITB- $\omega$  phase formed is due to the  
360 compression strains during the reversed martensitic transformation on the twinning  
361 boundaries.
- 362 (5) The sequence of deformation can thus be described as follow:
- 363 ① during loading, the  $\beta$  phase firstly transforms into  $\alpha''$  martensite; ② when this  
364 transformation is fully accomplished,  $\{1\ 1\ 0\}\langle 1\ 1\ 0\rangle_{\alpha''}$  twins are formed in the  $\alpha''$   
365 martensite during subsequent plastic deformation, as well as dislocation slip occurs; ③  
366 when the stress is removed from the plastic deformation range, the reverse transformation  
367 from  $\alpha''$  to  $\beta$  phase occurs; ④ the twins formed into  $\alpha''$  martensite reverse thus into a  
368 deformation band exhibiting a  $\{1\ 1\ 2\}\langle 1\ 1\ 1\rangle_{\beta}$  twinning relationship; ⑤ a thin layer of  $\omega$   
369 phase lying along the twin boundary (ITB  $\omega$  phase) is also formed in order to relax the stress  
370 accompanying this reverse transformation.

## 372 Acknowledgments

373 The authors acknowledge the European Synchrotron Radiation Facility for provision of  
374 synchrotron radiation facilities and would like to thank Yves Watier for assistance in using the  
375 beamline ID31. The authors also acknowledge Prof. Yulin Hao and Dr. Haoliang Wang in Institute  
376 of Metal Research Chinese Academy of Sciences for providing single crystal, and Dr. Guanglong  
377 Xu for the helpful discussion on the theory of phase transformation. This work was supported by  
378 Shenzhen Fundamental Research (JCYJ 20160427170611414).

## 379 References:

- 380 [1] J.A. Klostermann, The concept of the habit plane and the phenomenological theories of the martensite  
381 transformation, *Journal of the Less Common Metals* 28(1) (1972) 75-94.
- 382 [2] D.S. Lieberman, M.S. Wechsler, T.A. Read, Cubic to Orthorhombic Diffusionless Phase Change-  
383 Experimental and Theoretical Studies of AuCd, *Journal of Applied Physics* 26(4) (1955) 473-484.
- 384 [3] W. Sinkler, D. Luzzi, An electron diffraction investigation of the diffuse  $\omega$  structure in quenched Ti-3d  
385 transition metal alloys, *Acta Metallurgica et Materialia* 42 (1994) 1249-1260.
- 386 [4] P.D. Frost, W.M. Parris, D.L. Hirsh, J.R. Diog, C.M. Schwattz, Isothermal transformation of  
387 titanium-chromium alloys, *Transactions of the American Society for Metals* 46 (1954) 231-256.
- 388 [5] T. Yamamoto, K. Hayashi, N. Happo, S. Hosokawa, H. Tajiri, Local atomic structure near an Nb atom in aged  
389  $\beta$ -Ti alloys, *Acta Materialia* 131 (2017) 534-542.
- 390 [6] S. Shin, C. Zhang, K.S. Vecchio, Phase stability dependence of deformation mode correlated mechanical  
391 properties and elastic properties in Ti-Nb gum metal, *Materials Science and Engineering: A* 702 (2017) 173-183.
- 392 [7] L.M. Hsiung, D.H. Lassila, Shock-induced deformation twinning and omega transformation in tantalum and  
393 tantalum-tungsten alloys, *Acta Materialia* 48 (2000) 4851-4865.
- 394 [8] G.K. Dey, R. Tewari, S. Banerjee, G. Jyoti, S.C. Gupta, K.D. Joshi, S.K. Sikka, Formation of a shock  
395 deformation induced  $\omega$  phase in Zr 20 Nb alloy, *Acta Materialia* 52(18) (2004) 5243-5254.
- 396 [9] L.M. Hsiung, D.H. Lassila, Shock-induced displacive transformations in Tantalum and Tantalum-Tungsten  
397 alloys, *Acta Metallurgica* 39 (1998) 603-609.
- 398 [10] A. Devaraj, S. Nag, R. Srinivasan, R.E.A. Williams, S. Banerjee, R. Banerjee, H.L. Fraser, Experimental  
399 evidence of concurrent compositional and structural instabilities leading to  $\omega$  precipitation in titanium-  
400 molybdenum alloys, *Acta Materialia* 60(2) (2012) 596-609.
- 401 [11] D. Choudhuri, Y. Zheng, T. Alam, R. Shi, M. Hendrickson, S. Banerjee, Y. Wang, S.G. Srinivasan, H. Fraser,  
402 R. Banerjee, Coupled experimental and computational investigation of omega phase evolution in a high misfit  
403 titanium-vanadium alloy, *Acta Materialia* 130 (2017) 215-228.
- 404 [12] S.A. Mantri, D. Choudhuri, T. Alam, V. Ageh, F. Sun, F. Prima, R. Banerjee, Change in the deformation mode  
405 resulting from beta-omega compositional partitioning in a TiMo alloy: Room versus elevated temperature, *Scripta*  
406 *Materialia* 130 (2017) 69-73.
- 407 [13] H. Liu, M. Niinomi, M. Nakai, K. Cho, Athermal and deformation-induced  $\omega$ -phase transformations in  
408 biomedical beta-type alloy Ti-9Cr-0.2O, *Acta Materialia* 106 (2016) 162-170.
- 409 [14] H. Liu, M. Niinomi, M. Nakai, K. Cho, H. Fujii, Deformation-induced  $\omega$ -phase transformation in a  $\beta$ -type  
410 titanium alloy during tensile deformation, *Scripta Materialia* 130 (2017) 27-31.
- 411 [15] M. Tane, T. Nakano, S. Kuramoto, M. Niinomi, N. Takesue, H. Nakajima,  $\omega$  Transformation in cold-worked  
412 Ti-Nb-Ta-Zr-O alloys with low body-centered cubic phase stability and its correlation with their elastic  
413 properties, *Acta Materialia* 61(1) (2013) 139-150.
- 414 [16] J. Zhang, C.C. Tasan, M.J. Lai, A.C. Dippel, D. Raabe, Complexion-mediated martensitic phase  
415 transformation in Titanium, *Nature Communication* 8 (2017) 14210.
- 416 [17] M. Niinomi, M. Nakai, M. Hendrickson, P. Nandwana, T. Alam, D. Choudhuri, R. Banerjee, Influence of

- 417 oxygen on omega phase stability in the Ti-29Nb-13Ta-4.6Zr alloy, *Scripta Materialia* 123 (2016) 144-148.
- 418 [18] P. Castany, Y. Yang, E. Bertrand, T. Gloriant, Reversion of a Parent  $\{130\} \langle 310 \rangle$  alpha" Martensitic Twinning  
419 System at the Origin of  $\{332\} \langle 113 \rangle$  beta Twins Observed in Metastable beta Titanium Alloys, *Physical Review*  
420 *Letters* 117(24) (2016) 245501.
- 421 [19] M.J. Lai, C.C. Tasan, J. Zhang, B. Grabowski, L.F. Huang, D. Raabe, Origin of shear induced  $\beta$  to  $\omega$   
422 transition in Ti-Nb-based alloys, *Acta Materialia* 92 (2015) 55-63.
- 423 [20] B. Horovitz, J.L. Murray, J.A. Krumhansl, Stacking solitons in  $\omega$ -phase systems and quasielastic scattering,  
424 *Physical Review B* 18(7) (1978) 3549-3558.
- 425 [21] H. Xing, J. Sun, Mechanical twinning and omega transition by  $\langle 111 \rangle \{112\}$  shear in a metastable  $\beta$  titanium  
426 alloy, *Applied Physics Letters* 93(3) (2008) 031908.
- 427 [22] Y. Yang, G.P. Li, H. Wang, S.Q. Wu, L.C. Zhang, Y.L. Li, K. Yang, Formation of zigzag-shaped  $\{112\} \langle 111 \rangle$   
428 b mechanical twins in Ti-24.5 Nb-0.7 Ta-2 Zr-1.4 O alloy, *Scripta Materialia* 66(5) (2012) 211-214.
- 429 [23] L. Li, W. Mei, H. Xing, X.L. Wang, J. Sun, Zigzag configuration of mechanical twin and stress-induced  
430 omega phase in metastable  $\beta$  Ti-34Nb (at.%) alloy, *Journal of Alloys and Compounds* 625 (2015) 188-192.
- 431 [24] S.Q. Wu, D.H. Ping, Y. Yamabe-Mitarai, W.L. Xiao, Y. Yang, Q.M. Hu, G.P. Li, R. Yang,  $\{112\} \langle 111 \rangle$   
432 Twinning during  $\omega$  to body-centered cubic transition, *Acta Materialia* 62 (2014) 122-128.
- 433 [25] Y.L. Hao, Z.B. Zhang, S.J. Li, R. Yang, Microstructure and mechanical behavior of a Ti-24Nb-4Zr-8Sn  
434 alloy processed by warm swaging and warm rolling, *Acta Materialia* 60(5) (2012) 2169-2177.
- 435 [26] H. Zhan, G. Wang, D. Kent, M. Dargusch, The dynamic response of a metastable  $\beta$  Ti-Nb alloy to high strain  
436 rates at room and elevated temperatures, *Acta Materialia* 105 (2016) 104-113.
- 437 [27] X.L. Wang, L. Li, H. Xing, P. Ou, J. Sun, Role of oxygen in stress-induced  $\omega$  phase transformation and  
438  $\{332\} \langle 113 \rangle$  mechanical twinning in  $\beta$ Ti-20V alloy, *Scripta Materialia* 96 (2015) 37-40.
- 439 [28] Y. Yang, P. Castany, E. Bertrand, M. Cornen, T. Gloriant, Investigation of mechanical twinning in the  
440 Ti-24Nb-4Zr-8Sn b titanium alloy, *Proceedings of the 13th World Conference on Titanium* (2016) 1783-1786.
- 441 [29] O. Izumi, S. Hanada, Transmission electron microscopic observations of mechanical twinning in metastable  
442 beta titanium alloys, *Metallurgical Transactions A* 17 (1986) 1409-1420.
- 443 [30] E. Bertrand, P. Castany, I. Péron, T. Gloriant, Twinning system selection in a metastable  $\beta$ -titanium alloy by  
444 Schmid factor analysis, *Scripta Materialia* 64(12) (2011) 1110-1113.
- 445 [31] A. Ramarolahy, P. Castany, F. Prima, P. Laheurte, I. Peron, T. Gloriant, Microstructure and mechanical  
446 behavior of superelastic Ti-24Nb-0.5O and Ti-24Nb-0.5N biomedical alloys, *Journal of the Mechanical Behavior*  
447 *of Biomedical Materials* 9 (2012) 83-90.
- 448 [32] E. Sucedai, M. Shimoda, H. Nishizawa, Y. Nako, Nucleation Behaviour of beta to omega Phase  
449 Transformations in beta-Type Ti-Mo Alloys, *Materials Transactions* 52(3) (2011) 324-330.
- 450 [33] D.H. Ping, Review on  $\omega$  Phase in Body-Centered Cubic Metals and Alloys, *Acta Metallurgica Sinica (English*  
451 *Letters)* 27(1) (2014) 1-11.
- 452 [34] L.C. Zhang, D. Klemm, J. Eckert, Y.L. Hao, T.B. Sercombe, Manufacture by selective laser melting and  
453 mechanical behavior of a biomedical Ti-24Nb-4Zr-8Sn alloy, *Scripta Materialia* 65(1) (2011) 21-24.
- 454 [35] Y. Yang, P. Castany, M. Cornen, I. Thibon, F. Prima, T. Gloriant, Texture investigation of the superelastic Ti-  
455 24Nb-4Zr-8Sn alloy, *Journal of Alloys and Compounds* 591 (2014) 85-90.
- 456 [36] Y.J. Liu, X.P. Li, L.C. Zhang, T.B. Sercombe, Processing and properties of topologically optimised

- 457 biomedical Ti–24Nb–4Zr–8Sn scaffolds manufactured by selective laser melting, *Materials Science and*  
458 *Engineering: A* 642 (2015) 268-278.
- 459 [37] Y. Yang, P. Castany, M. Cornen, F. Prima, S.J. Li, Y.L. Hao, T. Gloriant, Characterization of the martensitic  
460 transformation in the superelastic Ti–24Nb–4Zr–8Sn alloy by in situ synchrotron X-ray diffraction and dynamic  
461 mechanical analysis, *Acta Materialia* 88 (2015) 25-33.
- 462 [38] H.L. Wang, Y.L. Hao, S.Y. He, K. Du, T. Li, E.G. Obbard, J. Hudspeth, J.G. Wang, Y.D. Wang, Y. Wang, F.  
463 Prima, N. Lu, M.J. Kim, J.M. Cairney, S.J. Li, R. Yang, Tracing the coupled atomic shear and shuffle for a cubic  
464 to a hexagonal crystal transition, *Scripta Materialia* 133 (2017) 70-74.
- 465 [39] H.L. Wang, Y.L. Hao, S.Y. He, T. Li, J.M. Cairney, Y.D. Wang, Y. Wang, E.G. Obbard, F. Prima, K. Du, S.J.  
466 Li, R. Yang, Elastically confined martensitic transformation at the nano-scale in a multifunctional titanium alloy,  
467 *Acta Materialia* 135 (2017) 330-339.
- 468 [40] P. Castany, A. Ramarolahy, F. Prima, P. Laheurte, C. Curfs, T. Gloriant, In situ synchrotron X-ray diffraction  
469 study of the martensitic transformation in superelastic Ti-24Nb-0.5N and Ti-24Nb-0.5O alloys, *Acta Materialia* 88  
470 (2015) 102-111.
- 471 [41] T. Grosdidier, M.J. Philippe, Deformation induced martensite and superelasticity in a b-metastable titanium  
472 alloy, *Materials Science and Engineering A* 291 (2000) 218–223.
- 473 [42] P. Castany, D.M. Gordin, S.I. Drob, C. Vasilescu, V. Mitran, A. Cimpean, T. Gloriant, Deformation  
474 Mechanisms and Biocompatibility of the Superelastic Ti–23Nb–0.7Ta–2Zr–0.5N Alloy, *Shape Memory and*  
475 *Superelasticity* 2(1) (2016) 18-28.
- 476 [43] G. Taylor, Thermally-activated deformation of BCC metals and alloys, *Progress in Materials Science* 36  
477 (1992) 29-61.
- 478 [44] P. Castany, M. Besse, T. Gloriant, In situ TEM study of dislocation slip in a metastable  $\beta$  titanium alloy,  
479 *Scripta Materialia* 66(6) (2012) 371-373.
- 480 [45] P. Castany, M. Besse, T. Gloriant, Dislocation mobility in gum metal  $\beta$ -titanium alloy studied via in  
481 situ transmission electron microscopy, *Physical Review B* 84(2) (2011).
- 482 [46] H. Tobe, H.Y. Kim, T. Inamura, H. Hosoda, S. Miyazaki, Origin of {332} twinning in metastable  $\beta$ -Ti alloys,  
483 *Acta Materialia* 64 (2014) 345-355.
- 484 [47] E. Bertrand, P. Castany, Y. Yang, E. Menou, T. Gloriant, Deformation twinning in the full- $\alpha''$  martensitic Ti–  
485 25Ta–20Nb shape memory alloy, *Acta Materialia* 105 (2016) 94-103.
- 486 [48] D.H. Ping, Y. Yamabe-Mitarai, C.Y. Cui, F.X. Yin, M.A. Choudhry, Stress-induced  $\alpha''$  martensitic (110)  
487 twinning in  $\beta$ -Ti alloys, *Applied Physics Letters* 93(15) (2008) 151911.
- 488 [49] Y.W. Chai, H.Y. Kim, H. Hosoda, S. Miyazaki, Self-accommodation in Ti–Nb shape memory alloys, *Acta*  
489 *Materialia* 57(14) (2009) 4054-4064.
- 490 [50] R.W. Cahn, Plastic deformation of alpha-uranium twinning and slip, *Acta Metallurgica* 1 (1953) 49-70.
- 491 [51] A.G. Crocker, The crystallography of deformation twinning in alpha-uranium, *Journal of Nuclear Materials*  
492 16 (1965) 306-326.
- 493 [52] R.D. Field, R.J. McCabe, D.J. Alexander, D.F. Teter, Deformation twinning and twinning related fracture in  
494 coarse-grained  $\alpha$ -uranium, *Journal of Nuclear Materials* 392(1) (2009) 105-113.
- 495 [53] T. Inamura, J.I. Kim, H.Y. Kim, H. Hosoda, K. Wakashima, S. Miyazaki, Composition dependent  
496 crystallography of  $\alpha''$ -martensite in Ti–Nb-based  $\beta$ -titanium alloy, *Philosophical Magazine* 87(23) (2007)

497 3325-3350.

498

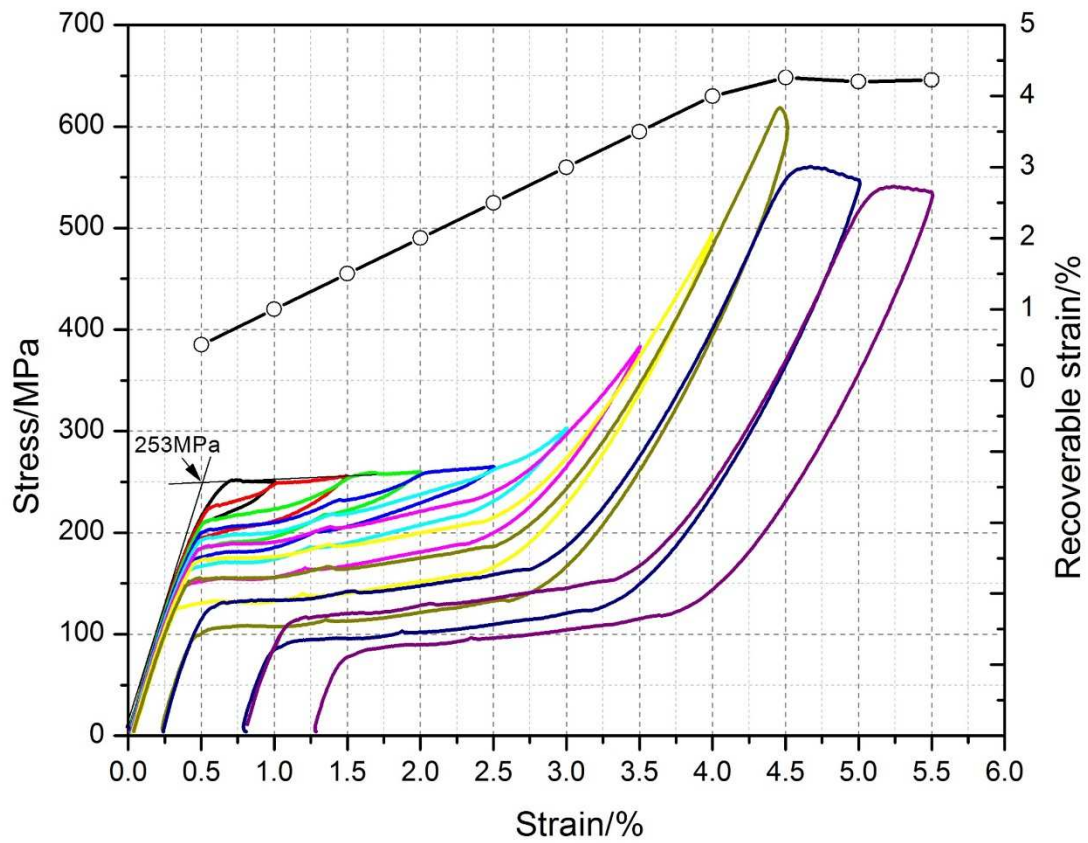
ACCEPTED MANUSCRIPT

Table 1. Cell parameters of different phases after releasing stress at higher applied strain in the plastic deformation range.

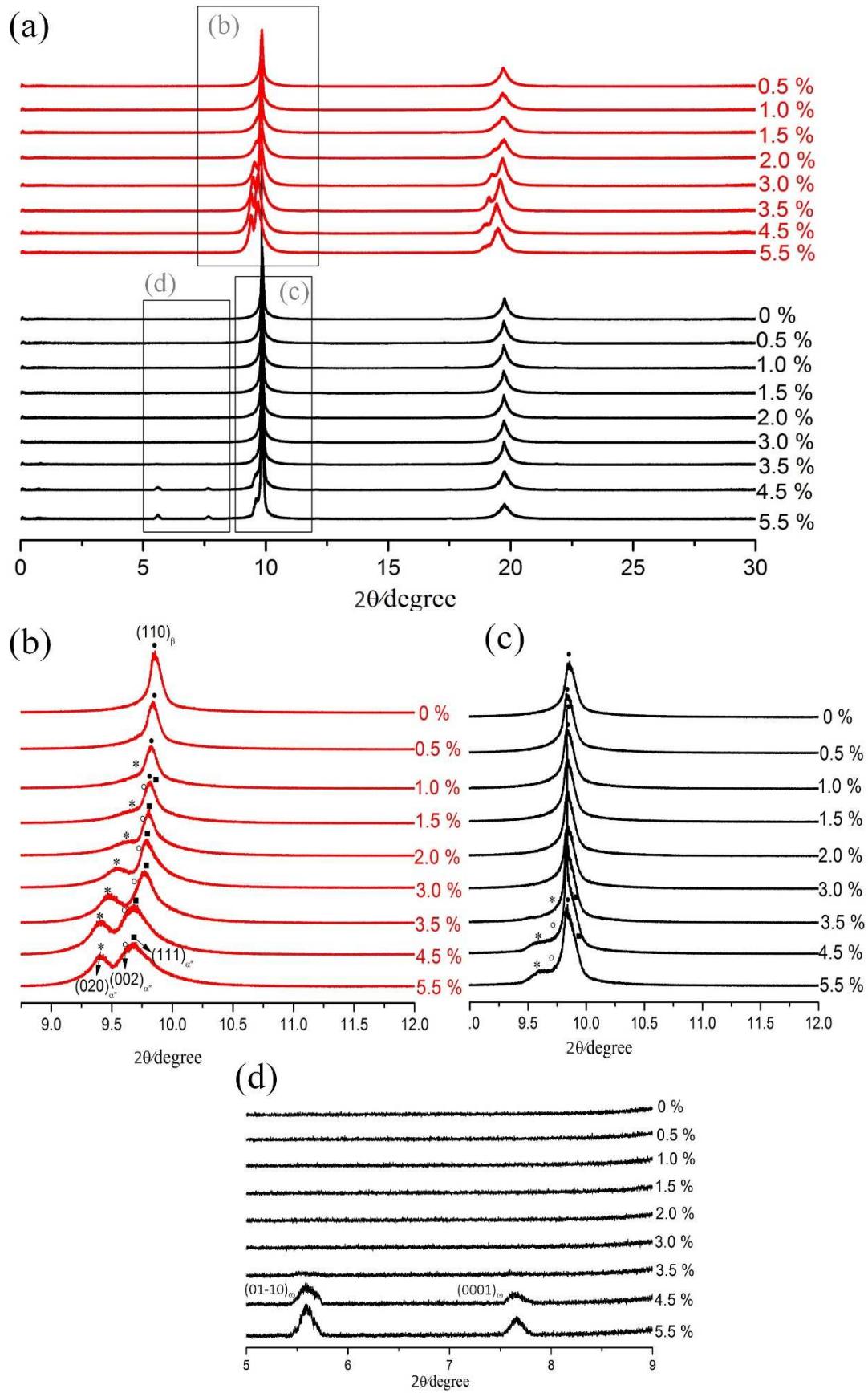
Cell parameters (Å)	loading		Unloading			
	SIM $\alpha''$ phase		$\beta$ phase		$\omega$ phase	
	4.5 %	5.5 %	4.5 %	5.5 %	4.5 %	5.5 %
a	3.261	3.260	3.298	3.298	4.732	4.732
b	4.864	4.865			4.732	4.732
c	4.848	4.851			2.991	2.991

Table 2. The six lattice correspondence of variants for martensitic  $\alpha''$  phase derived from the parent  $\beta$  phase and the calculated strain of phase transformation at the external loading direction of  $[1\ 0\ 1]_{\beta}$ .

Variants correspondence	$[100]_{\alpha''}$	$[010]_{\alpha''}$	$[001]_{\alpha''}$	Transformation strain along the loading direction of $[101]_{\beta}$	
				Applied strain of 4.5%	Applied strain of 5.5%
CV1	$[100]_{\beta}$	$[011]_{\beta}$	$[0\bar{1}1]_{\beta}$	1.50	1.50
CV2	$[100]_{\beta}$	$[0\bar{1}1]_{\beta}$	$[0\bar{1}\bar{1}]_{\beta}$	1.50	1.50
<b>CV3</b>	<b><math>[010]_{\beta}</math></b>	<b><math>[101]_{\beta}</math></b>	<b><math>[10\bar{1}]_{\beta}</math></b>	<b>4.29</b>	<b>4.31</b>
CV4	$[010]_{\beta}$	$[10\bar{1}]_{\beta}$	$[\bar{1}0\bar{1}]_{\beta}$	3.94	4.01
CV5	$[001]_{\beta}$	$[110]_{\beta}$	$[\bar{1}10]_{\beta}$	1.50	1.50
CV6	$[001]_{\beta}$	$[\bar{1}10]_{\beta}$	$[\bar{1}\bar{1}0]_{\beta}$	1.50	1.50



**Fig. 1.** Cyclic tensile curve of the single crystal Ti-24Nb-4Zr-8Sn alloy with the corresponding measured recoverable strains (open circles).



**Fig. 2.** Synchrotron X-ray diffraction profiles of the single crystal Ti-24Nb-4Zr-8Sn alloy: (a) the full diffractograms on loading and corresponding unloading and (b-d) enlarged partial diffractograms marked in (a) with precise indexing.

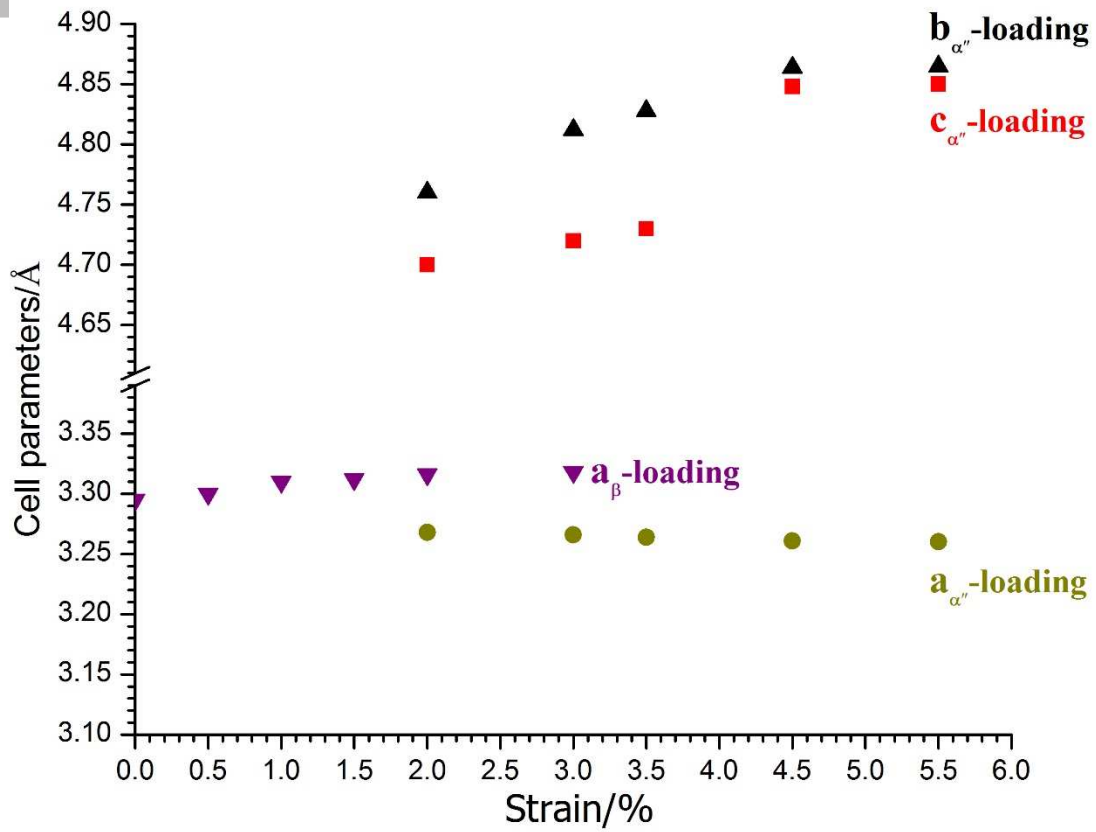


**Fig. 3.** Evolution of the cell parameters of the different phases determined from the SXRD profiles.

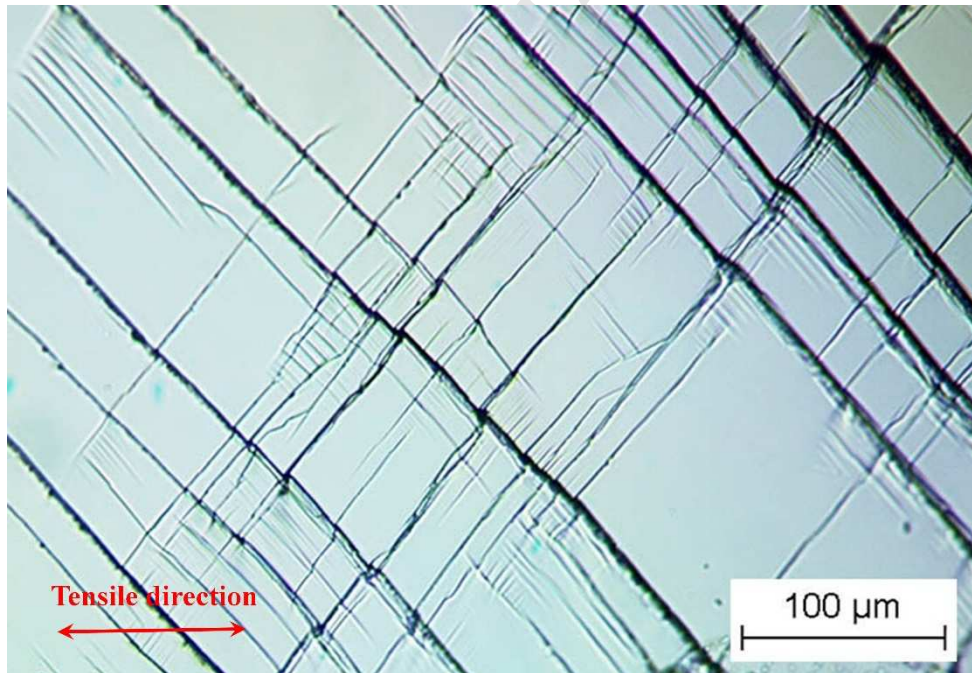


**Fig. 4.** Optical microstructure of the single crystal Ti-24Nb-4Zr-8Sn alloy after deformation up to 4.5 % strain.

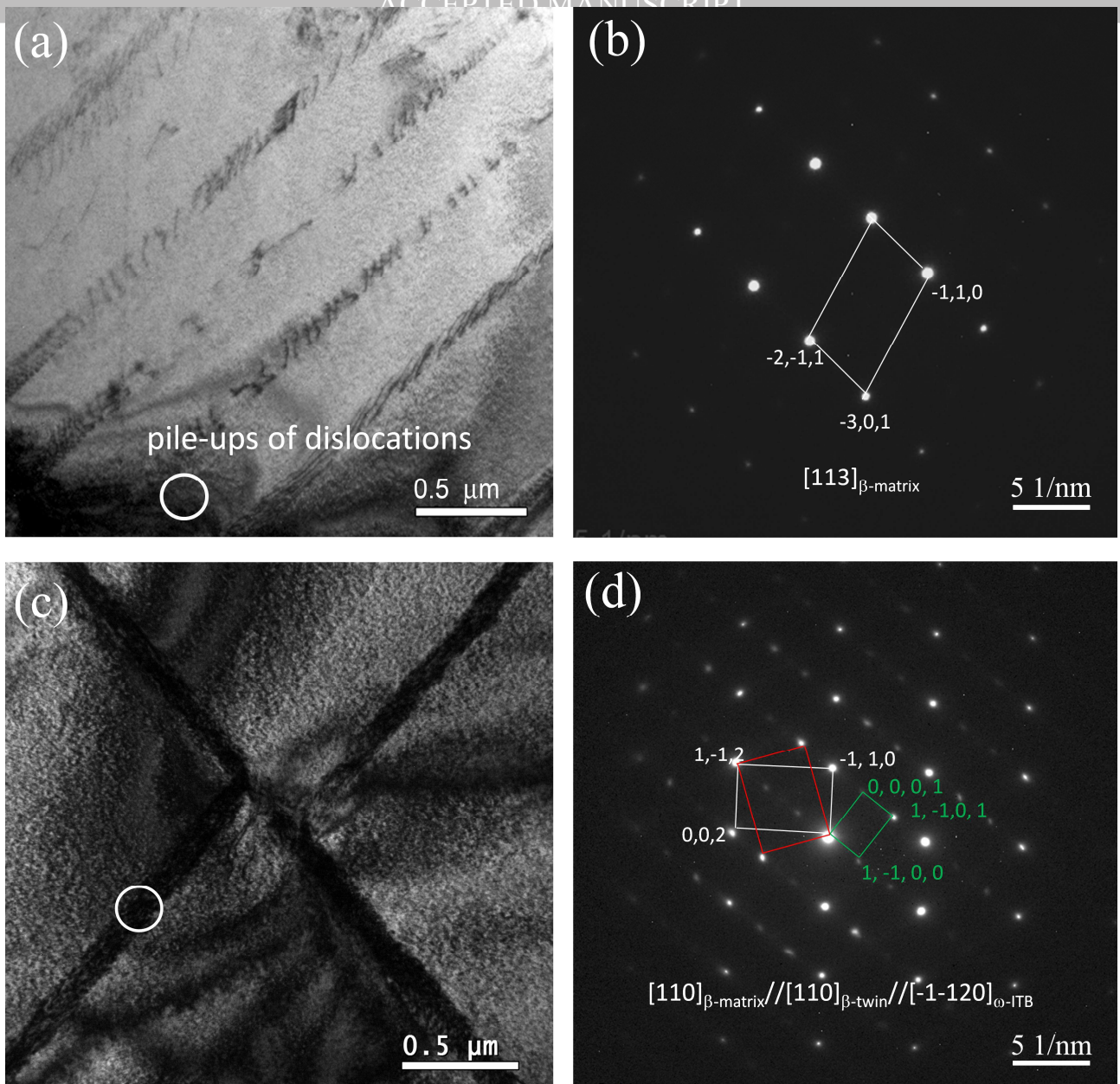


**Fig. 5.** TEM observations of the sample deformed up to 4.5 % strain: (a) pile-ups of dislocations and (b) corresponding selected diffraction pattern of the area marked by white circle in (a); (c) two deformation bands crossing with each other and (d) the selected diffraction pattern of the area marked by white circle in (c).

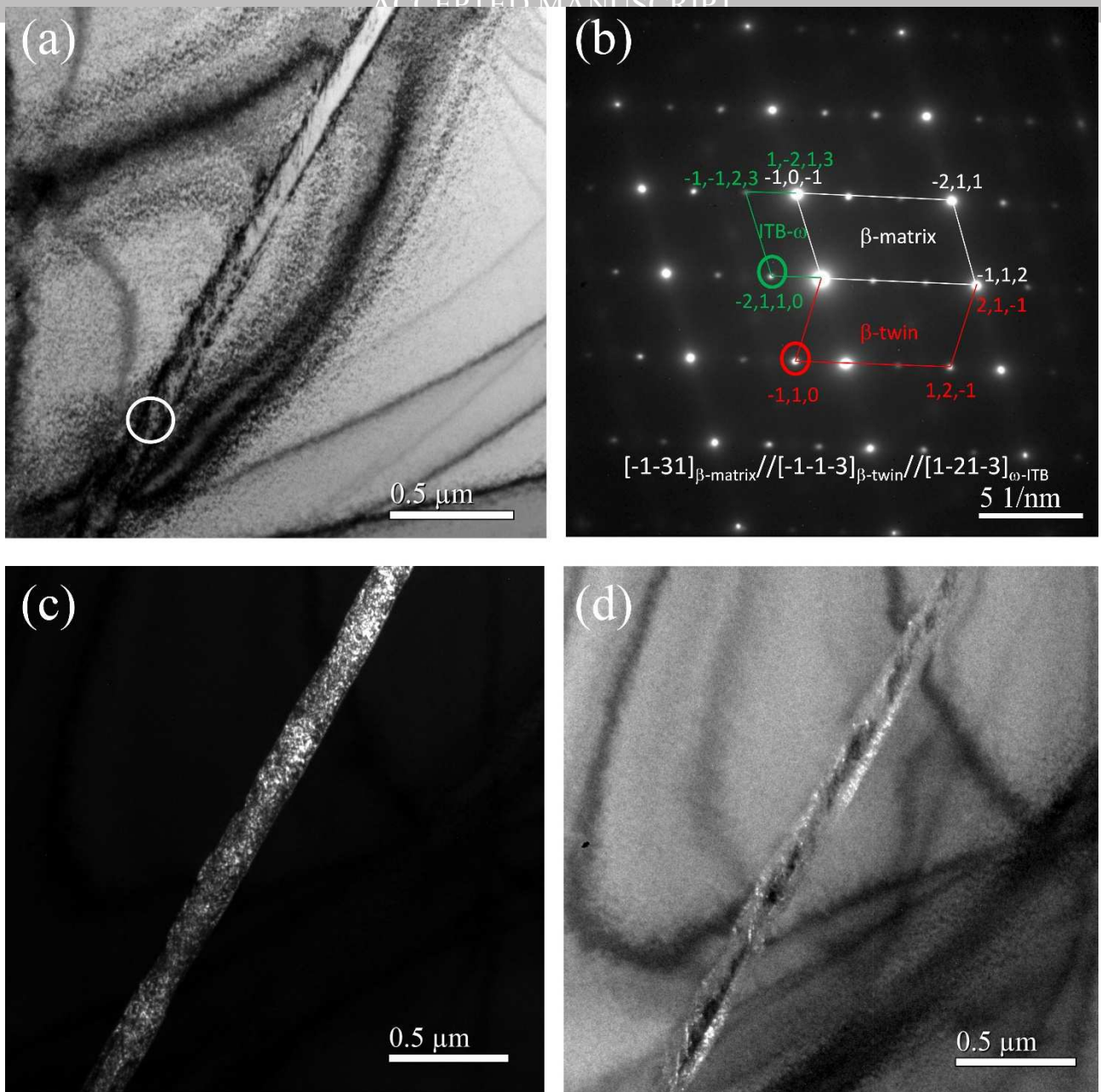


**Fig. 6.** TEM observations of one single deformation band for the sample deformed up to 4.5 % strain: (a) bright field image and (b) the corresponding selected area diffraction patterns; (c) and (d) the dark field images taken with the spots highlighted by red and green circles in (b) corresponding to  $(-1\ 1\ 0)_{\beta}$  and  $(-2\ 1\ 1\ 0)_{\omega}$ , respectively.

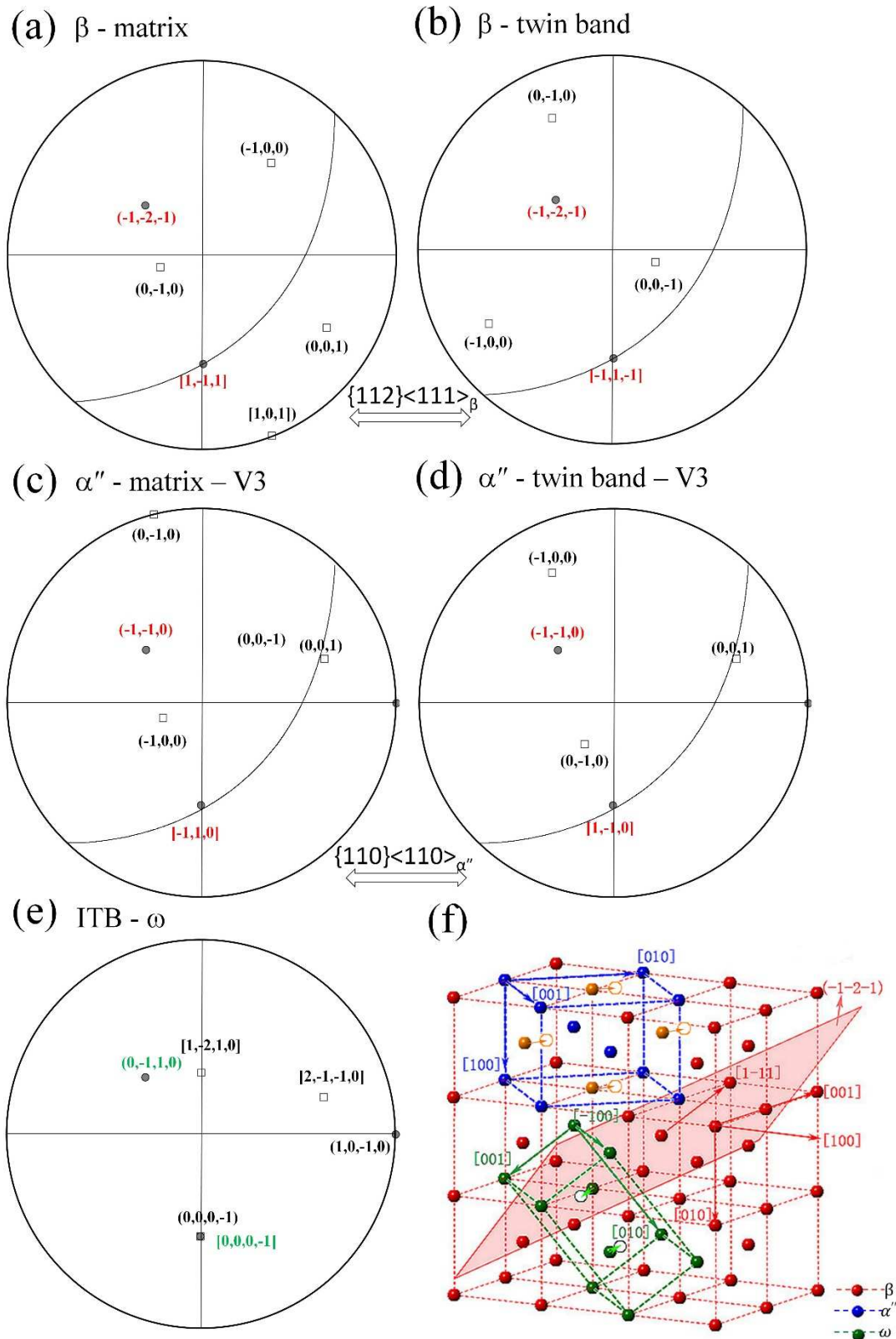
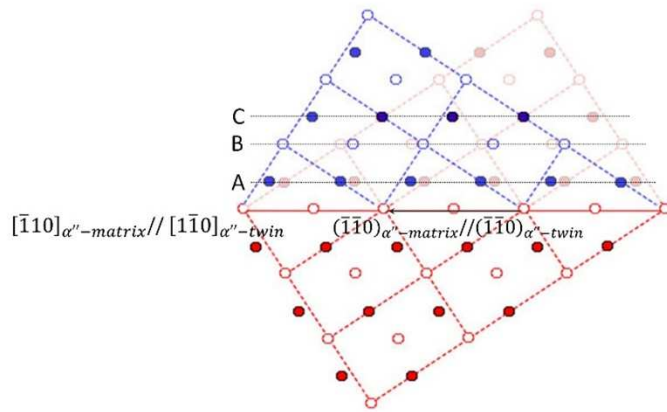
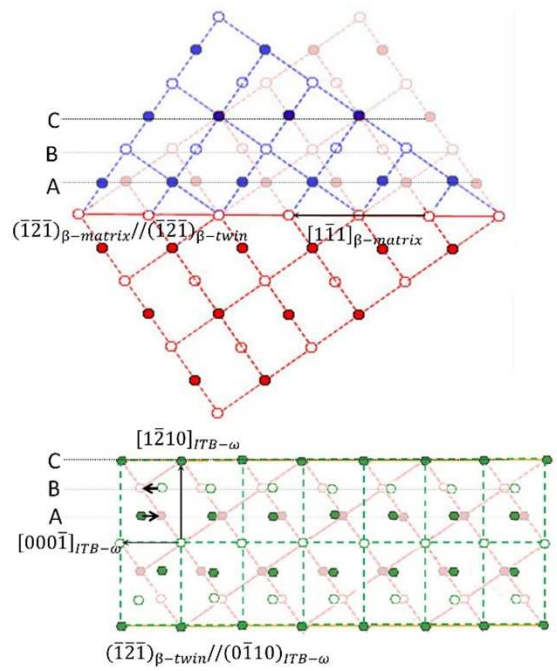


**Fig. 7** Crystallographic orientations represented as stereographic projections used to determine the orientation relationship between the matrix and twin shown in Fig. 6: the  $(-1\ -1\ -2)[1\ -1\ 1]_{\beta}$  twinning relationship between the  $\beta$ -matrix (a) and the  $\beta$ -twin band (b); the compound  $(-1\ -1\ 0)[1\ 1\ 0]_{\alpha''}$  twinning relationship between the  $\alpha''$ -matrix-V3 (c) and the  $\alpha''$ -twin band-V3 (d); (e) the orientation of ITB- $\omega$  phase and (f) the lattice correspondence of  $\beta$ -matrix,  $\alpha''$ -matrix-V3 and ITB- $\omega$  phase.

(a) loading



(b) unloading



(c) unloading

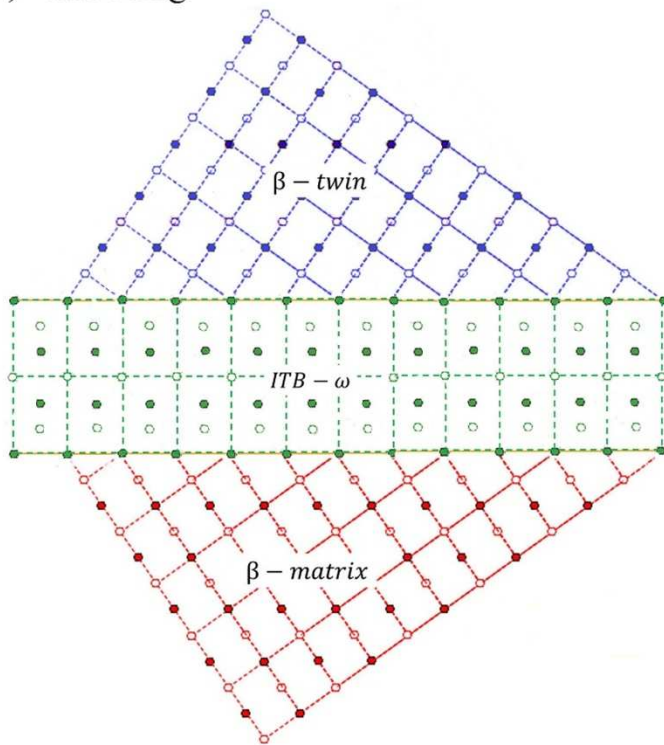


**Fig. 8** Schematic illustration of orientation relationships for single crystal Ti-24Nb-4Zr-8Sn alloy: (a) the compound  $(-1 -1 0)[-1 1 0]_{\alpha'}$  twinning relationship on loading, (b) the  $(-1 -1 -2)[1 -1 1]_{\beta}$  twinning relationship and formation of ITB- $\omega$  after unloading and (c) the whole reversed morphology under unloading condition.